Miniature Parallel Continuum Robot Made of Glass: Analysis, Design, and Proof-of-Concept

Chibundo Nwafor, Guillaume J. Laurent, and Kanty Rabenorosoa, *Member, IEEE*

Abstract—Parallel continuum robots (PCRs) are flexible manipulators, whose configuration is determined by the controlled deformation of their parallel-arranged elastic links. They are of great interest for micro-manipulation applications due to their intrinsic compliance, their extrinsic actuation, and their miniaturization potential. This paper presents the design and prototype of a miniature 3-DoF glass PCR, capable of reaching large tip-tilt angles in a tiny volume. The flexible structure is composed of 3 legs made of glass, each one having an extension range from 6 to 15 mm and a diameter of 125 μm. The workspace of the robot, its stiffness, and manipulability are evaluated with respect to varying geometrical proportions of the platform size with respect to the base diameter. Experimental validation shows that the platform is able to reach tip-tilt angles from -84° to 117° in a space of 15 mm wide and 10 mm high and to follow conveniently desired paths within its workspace.

I. INTRODUCTION

Miniaturized manipulators are designed to manipulate small objects with a high degree of accuracy and repeatability in confined spaces. These devices have a wide range of applications in different fields, such as manipulation inside scanning electron microscopes (SEM), and endoscopic medical procedures. Within a SEM, miniaturized manipulators are used for handling samples for imaging, performing various measurements, or assembling components. In endoscopic medical procedures, the manipulators are inserted into the body through small incisions and are used to perform delicate procedures, such as imaging, biopsy, suturing, or removing small tissue samples. One of the current challenges of micromanipulation e.g in SEM or medical is to increase the dexterity of the manipulators by integrating rotations at the distal end to actualize tool orientation with large angles. Indeed, the three translational movements of the end effector in the $x-$, $y-$, and $z-$axis, can be generated by proximal joints, whereas only distal ones can produce the orientation of the tool. Having a distal orientation section is well known to improve manipulator dexterity [1]–[4].

To that effect, parallel manipulators have many advantages such as high precision, high speed, and extrinsic actuation that enables locating the actuators outside of the confined space leading to a very high miniaturization potential. Presently, the smallest parallel manipulators in the literature include Millidelta [5] and Migribot [6]. Though each presents key benefits thanks to their parallel configurations, they are both
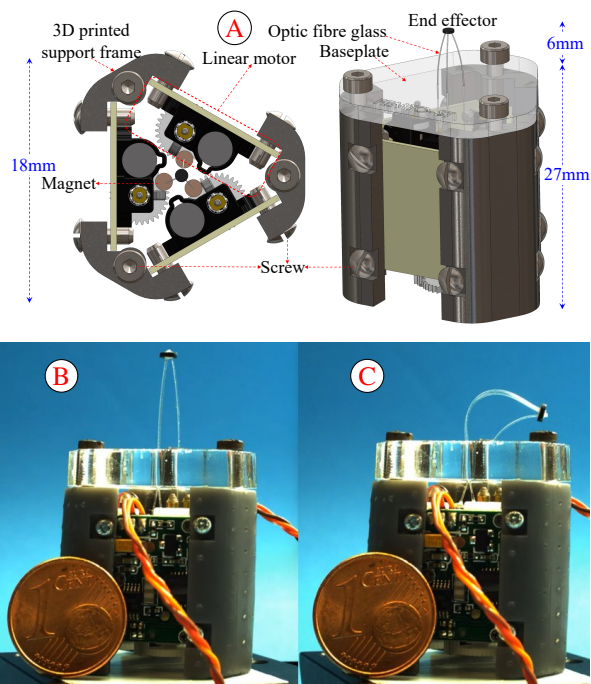
Fig. 1. The miniaturized PCR made of glass, **A)** Computer-aided design (CAD) of the entire robot and its different components **B)** Prototype of the robot in maximal extension configuration **C)** Prototype of the robot in maximal bending configuration.

restricted to translative motion. Conversely, this issue and limitation can be solved using a new type of parallel robot called parallel continuum robots (PCRs) [7].

PCRs are members of the continuum robots family, and are composed of parallel flexible limbs and actuated at their proximal end. Their benefits are related to their high miniaturization potential because (1) no joints are required, (2) their structures can be compact, and (3) they can be extrinsically actuated. They also possess better stress distributions and large deformations than compliant structures, while maintaining their high scalability and large workspace [8]. These advantages open up opportunities for the design of many PCR manipulators of all sizes. Generally, PCRs can be classified as either planar [9]–[11] or non-planar with three limbs [12], [13] or six limbs [7], [14], [15]. Although they can also be classified based on their actuation e.g pneumatic [12], [16], SMA [17], tendon-actuated [11] or motorized [8], [14], [15]. Currently, the smallest PCR by footprint (all links and actuation unit) is the SMA manipulator ($30 \times 30 \times 34$mm) [17] that is able to tilt a maximum angle of 30°and to extend in z-axis up to 12 mm.

Therefore, to tackle the limitation and challenge of large workspace/rotation associated with miniaturized parallel manipulators in the literature, we present the smallest PCR

ROD MODEL (Cosserat Rod Equations)

$$v = v^* + K_{se}^{-1} R^T n$$
$$u = u^* + K_{bt}^{-1} R^T m$$
$$p' = Rv$$
$$R' = R\hat{u}$$
$$n' = -f$$
$$m' = -p' \times n - l$$

Where:
$'$: Derivative w.r.t arc-length
v: Link linear rate of change
v^*: Link at stress-free state
u: Link curvature
u^*: stress-free state curvature
$\hat{}$: Convert $\mathbb{R}^3$ to $\mathfrak{so}(3)$
n: Internal force
m: Internal moment
p: Position in arc-length
R: Rotation in arc-length
f: Distributed force/weight
l: Distributed moment
K_{se}^{-1}: Shear & extension stiffness matrix
K_{bt}^{-1}: Bending & torsion stiffness matrix

PCR MODEL

$$p_i(0) = r_b[cos\theta_i^b, sin\theta_i^b, 0]^T$$
$$r_i = r_e[cos\theta_i^e, sin\theta_i^e, 0]^T$$
$$p_i(L_i) = p_e + R_e r_i$$
$$[\log(R_i(L_i)^T R_e)]^v = 0$$
$$F = \sum_{i=1}^{3} n_i(L_i)$$
$$M = \sum_{i=1}^{3} [m_i(L_i) + R_e^T r_i \times n_i(L_i)]$$

Where: $L_i = L_i^* + q_i$
$\check{}$: Covert $\mathfrak{so}(3)$ to $\mathbb{R}^3$
i: Link indexing ($i \in [1,3]$)
θ_i^b: Angle between links at base
θ_i^e: Angle between links at end effector
p_e: End effector centroid position
R_e: End effector centroid orientation
r_b: Base radius from centroid
r_e: End effector radius from centroid
F: Applied force at the end effector
M: Applied moment at the end effector
L: Rod length from base to end effector
L^*: Rod length at minimum actuation
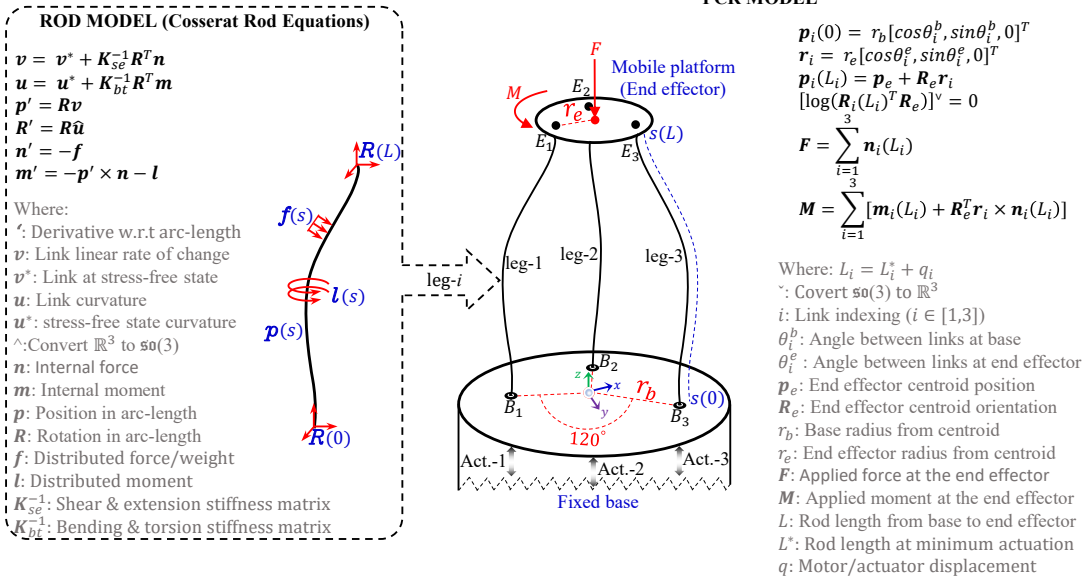q: Motor/actuator displacement

Fig. 2. The schematic of the 3-leg glass PCR and its modeling using the Cosserat rod formulation along with the boundary conditions.

capable of generating rotations over 90° of the end effector in a tiny volume. In addition, while the vast majority of PCRs use beams and rods of metal due to their flexibility and availability, the proposed prototype uses optical glass fibers, which have the benefits of high elasticity, small diameter, and the possibility of using them to transmit energy to an active end effector. Thus, the proposed miniaturized PCR has 3-DoFs (orientation in tip/tilt angles and the end effector contraction/extension), which were actualized using 3 glass optical fibers arranged in 120° apart. Its miniaturized design could permit integration onto an endoscope or multi-backbone robot tip for enhanced dexterity in micro-manipulation operation. One key possible application of the proposed PCR is the sample handling under SEM which will benefit from the large tip and tilt angles of the end-effector in a tiny volume.

In this paper, we investigated in detail the effect of the geometrical parameters of the robot in terms of the achievable workspace, stiffness, and manipulability and also, assessed experimentally the workspace and the model on path followings. The paper is organized as follows, Section II explains the robot concept and modeling while Section III presents the analysis of the robot design. The geometrical analysis of the robot was discussed in Section IV, followed by experimental validation in Section V, and finally, Section VI summarizes the conclusion and perspectives.

II. ROBOT ARCHITECTURE AND MODELING

A. Architecture

The schematic of the 3-leg miniaturized glass PCR is shown in Fig. 2. Basically, the components of the robot's mechanical structural design include:

1) End effector: this is located at the distal end of the robot, which can also be called the mobile platform. It is usually used to hold the robot link in position at the top and could be functionalized for a target application. The design shape of the end-effector is circular with a circumradius r_e.

2) Rods: this consist of three straight and flexible standard glass optical fibers $i \in [1, 3]$, which are called the robot links or legs. While one end is fixed to the end-effector, the other is connected to the linear actuator below the fixed base (Fig. 2). The region above the fixed base is called the robot's flexible part because the robot configuration depends on the link deformation upon actuation. The different rod lengths are used to actualize different robot configurations such as neutral configuration and bending configuration. The movement from one neutral configuration to another is used to actualize linear robot translation/displacement in the z-axis.

3) Fixed base or Base frame: this comprises the base structure that gives fixed stable support to the robot and provides the path through which each optical fiber passes when actuated. The hole design pattern is given in Cartesian coordinate at points B_1, B_2 and B_3, which are arranged 120° apart on a circumradius of r_b (Fig. 2).

4) Linear actuators: This provides the linear translation of each link, with an actuation range $l \leq q_i \leq L$, for $i \in [1, 3]$. In addition, this also provides the support upon which the rods are attached. The different robot configurations and end effector poses are achieved by varying the different linear joints q_i.

B. Modeling

For predicting the pose/configuration of a PCR, a geometrical exact model is important. To model the proposed miniaturized 3-leg glass PCR, we applied the modeling framework proposed in [8], [18], which treats a PCR as a boundary value problem (BVP). With the Cosserat rod mechanics framework [19], a rod can be described by a 12×1 vector of twist and wrench along its arc length. Additional constitutive laws relating to the kinematics variables and material strain (bending, torsion, shear, and extension) are also considered. These were all included for the robot modeling as concisely shown in Fig. 2. One can refer to [8], [18] for more details.

The shooting method has been used for solving the BVP model. This numerical approach comes with the price of convergence problem and computational burden for its accuracy but the same model formulation can be used for both the forward kinematic model (FKM) and the inverse kinematic model (IKM). The shooting method iteratively updates the guess values of the unknowns and output variables until the boundary conditions are satisfied within the solver tolerance. The non-linear optimization solver makes use of the Levenberg-Marquardt/Trust-Region-Dogleg algorithm while using the "ode45" MATLAB function to numerically integrate the rod, for each nested loop.

III. ROBOT DESIGN ANALYSIS

The robot design is highly dependent on the geometrical parameters and choice of materials, for the obtainable workspace/pose, manipulability, and stiffness. We investigated the different design variables, which are analyzed in detail below.

A. Workspace

The workspace is the volume enclosure reachable by the PCR end-effector position p_e and orientation R_e, for the different obtainable configurations. These are obtained by sampling iteration of the input variable q_i. The workspace is derived as the pose (position and orientation) of the end effector centroid with respect to each robot's configuration, for different discretized iterations of actuation links q_i. For each iteration of q_i, the FKM is computed via the shooting method, which derives the end effector centroid pose from the boundary conditions defined by the actuator positions. Using the material property of a standard single-mode optical fiber with 125μm diameter and imposing robot geometrical parameters of $r_e = 0.5mm$, $r_b = 5r_e$, $l_i = 12r_e$ and $q_i = 18r_e$, just like the experimental prototype. We evaluated the workspace of the PCR in the vertical x-axis plane at $x = 0$, the vertical y-axis plane at $y = 0$, and the horizontal plane cut at $z = 8$mm respectively. The q_i within the vertical and horizontal plane cut of the workspace is then used further to analyze the stiffness, Jacobian, and pose of the robot end effector centroid for the different configurations in the selected plane, as presented in Fig. 3. For better visualization and detailed analysis with regard to the evolution of the PCR variables under investigation, q_i iterates for 27,000 different combinations of sample points. Fig. 3A presents the entire workspace of the miniaturized PCR, which covers a volume space of $1174mm^3$. The result from the top view or the horizontal plane cut of the PCR workspace depicts a boundary shape of a "Reuleaux triangle".

B. Stiffness

The stiffness represents the robot's resistance to an externally applied wrench, which comprises a force F and a moment M (refer to Fig. 2). This analysis is useful to understand the load-carrying capacity of the PCR for the robot configuration within its workspace. Though the focus of this
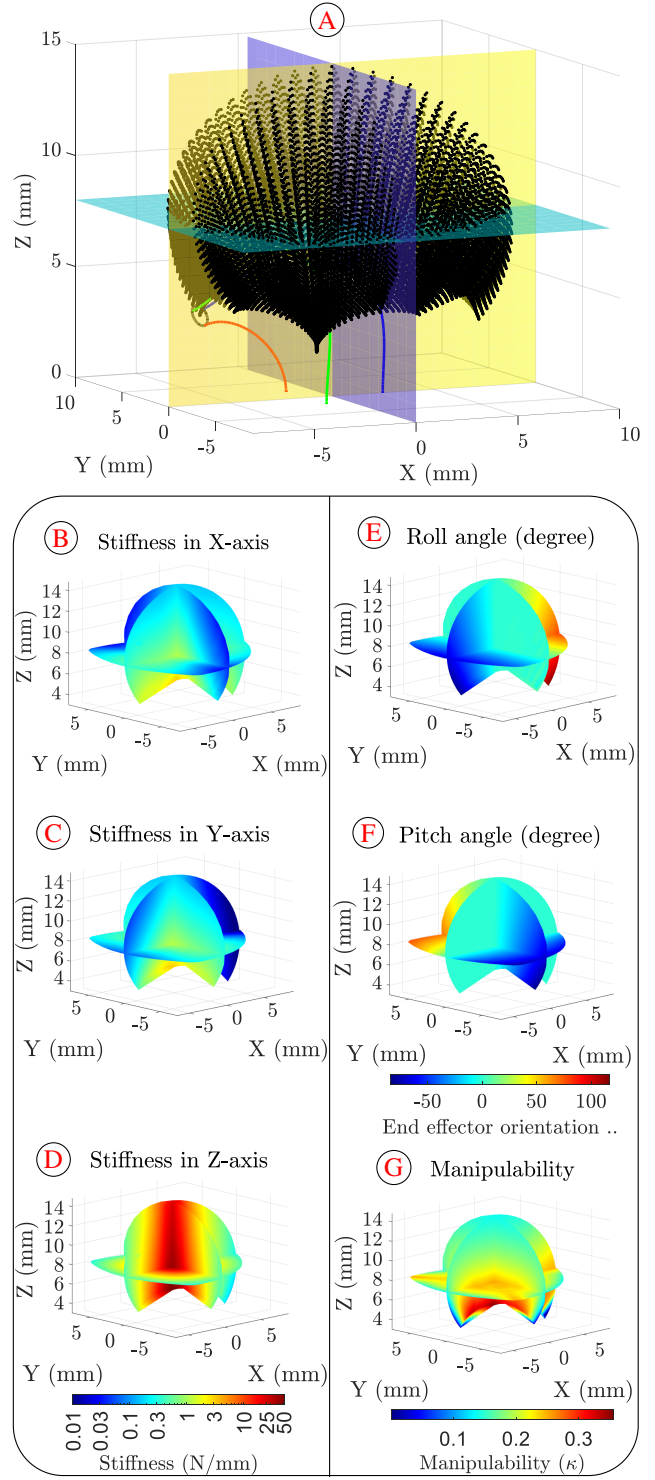

Fig. 3. Workspace of the miniature glass PCR: **A)** 3D volume of the entire workspace of the robot, **B) - D)** stiffness along the x-axis, y-axis, and z-axis respectively, **E)** robot manipulability in terms of condition number, **F) & G)** platform orientations.

paper is basically on the robot stiffness due to an applied force. In that regard, we investigated the stiffness for the various plane cuts of the workspace. The comparative result for the different stiffness when a small force is applied in $x-, y-$, and $z-$axis is presented in Fig. 3B, 3C, & 3D respectively. Generally, each of the results obtained shows that the stiffness

significantly varies with respect to the configuration of the robot within the workspace and also on the direction of the applied force F e.g in x-direction (Fig. 3B), y-direction (Fig. 3C) or in z-direction (Fig. 3D). The stiffness matrix $\boldsymbol{K}$ for each of the robot configurations within the workspace is computed by the finite difference approach, by observing the change in end-effector position $\boldsymbol{p}_e$ due to the small incremental change in the applied force $\triangle F_i$, as given in Eq. 1 below.

$$K \approx \begin{bmatrix} \dfrac{\boldsymbol{p}_e - \boldsymbol{p}_e^*}{\triangle F_x} & \dfrac{\boldsymbol{p}_e - \boldsymbol{p}_e^*}{\triangle F_y} & \dfrac{\boldsymbol{p}_e - \boldsymbol{p}_e^*}{\triangle F_z} \end{bmatrix} \quad (1)$$

Analyzing the stiffness when the force is applied in the $x-, y-$, and $z-$axis shows that the stiffness in the z-axis is the maximum and almost 15 times those in the $x-$ and $y-$axis. Generally for each case, the stiffness is maximum around the central bottom and then spread radially to the boundary of the workspace, where they are minimum. Considering Fig. 3B where the applied force is in the z-axis, one would observe that the stiffness is always maximum at the central axis for the neutral configurations (all links equal) and then decreases as the robot tilt or bend away from this axis towards the boundary of the workspace. The stiffness value for each point in the workspace when the force is applied in x and y-axis are not the same, this is due to the robot leg arrangement, where leg-1 is aligned on the x-axis while leg-2 and leg-3 are aligned at $120°$ apart. Therefore, the arrangement of the leg pattern influences the stiffness for the different configurations with respect to the applied force direction, as this is seen as the color gradient in Fig. 3B and Fig. 3C for $x-$ and $y-$direction respectively.

The end effector mass is 5.8mg and using a simple mass-spring system, its natural frequencies are about 2kHz in X and Y directions (taking the stiffness from Fig. 3 at the center of the horizontal cut $z = 8$). This is considerably higher than the bandwidth of the micro servomotor which is given to travel 9.1mm in 0.14s.

C. End Effector Orientation

The end effector orientation is computed for the different robot configurations within the various plane cuts in the workspace. The roll angle is taken as the rotation about the x-axis as Fig. 3E presents the color map of the obtainable roll angle, for the different robot configurations within the workspace. From the color gradient, one will notice that all the roll angles are 0 in the vertical cut plane at $x = 0$. Whereas it spreads radially in the other planes, which has a value of $+117°$ to $-82°$. For the pitch angle, Fig. 3F presents the color gradient for the variation of the end-effector rotation about the $y-$axis. Again, one will see that the pitch angle for all points in the $y-$axis is 0, whereas for $x-$axis its value ranges between $\pm84°$. The result of the design analysis is very important in terms of visualizing the different obtainable orientations in roll and pitch angles within the workspace.

D. Manipulability

Manipulability is the measure of the robot's motion capability at a given configuration. To investigate the manipulability of the miniature glass PCR, we evaluated the condition number at every configuration in the sampled points within the workspace.

Here, we used the 2-norm condition κ of the Jacobian matrix $\boldsymbol{J}$, given in Eq. 2.

$$\kappa = \sqrt{\frac{\lambda_{min}(\boldsymbol{J}^T\boldsymbol{J})}{\lambda_{max}(\boldsymbol{J}^T\boldsymbol{J})}} \quad (2)$$

where λ_{max} and λ_{min} are the largest and smallest eigenvalues of $\boldsymbol{J}^T\boldsymbol{J}$ respectively. With this measure, if the condition number approaches 1, this denotes high manipulability. If it approaches 0, it denotes less manipulability and toward singularity configuration which occurs at 0. The Jacobian matrix $\boldsymbol{J}$ used for the robot manipulability analysis is computed by observing the change in the end effector position $\boldsymbol{p}_e$ due to a small increment in the joint values q_i. The finite difference approach was used (Eq.3), where each ith column of the Jacobian is computed by increasing the joint input q_i by a small amount.

$$J \approx \begin{bmatrix} \dfrac{\boldsymbol{p}_e - \boldsymbol{p}_e^*}{\triangle q_1} & \dfrac{\boldsymbol{p}_e - \boldsymbol{p}_e^*}{\triangle q_2} & \dfrac{\boldsymbol{p}_e - \boldsymbol{p}_e^*}{\triangle q_3} \end{bmatrix} \quad (3)$$

The result for the overall computation for the different robot configurations within the workspace, when considering the three-plane cut is presented in Fig. 3G. It shows that the manipulability of the robot is maximum at the central bottom region and decreases radially within the workspace as the robot moves further away towards the boundary.

IV. GEOMETRICAL DESIGN PARAMETER ANALYSIS

The two main considerations for designing a PCR are the material properties and then, the geometrical parameters of the robot. The material properties relate to the inherent properties of the material, for the active part of the PCR e.g Young's modulus and Poisson ratio which depends on the type of material. Whereas, the geometrical parameter relates to the material dimension, geometric shape, and sizes, along with coupling or structural design. Since we are focused on the use of one material (glass optical fiber), therefore the major analysis is on the effect of the PCR geometrical parameters. The arc length is one of the geometrical key parameters for the PCR design. Another geometrical key parameter of consideration is the effect of the end-effector dimension since this represents the output section of the robot ($\boldsymbol{p}_e$ and $\boldsymbol{R}_e$). Therefore, we investigated the effect of the actuation length and the end-effector dimension, which are detailed below.

A. Actuation length parameter

The variation in the actuation length (linear translation), changes the arc length of the robot. It is very important to analyze the effect of the actuation length, which relates to the variation of arc length that results in the corresponding change of the robot backbone configuration. This is very crucial to PCR design because this parameter helps to determine or easily infer 1) the area of reachable workspace e.g L_1, L_2, L_3, L_4, L_5 and L_6, 2) the stable or maximum safe region of operation e.g see Figure 4 and lastly, 3) the region
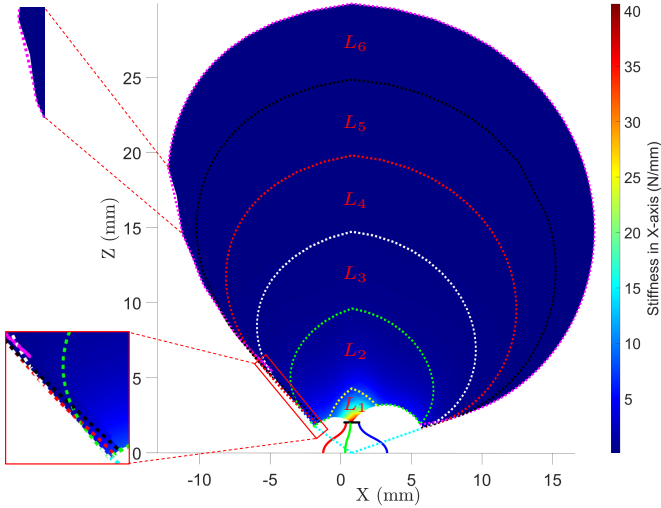
Fig. 4. Vertical plane cut workspace of the miniature glass PCR considering the effect of the actuation length which relates to the robot arc length. Projected areas are unstable regions due to negligible stiffness in long actuation length (see Table I for corresponding values).

TABLE I
THE DIFFERENT ACTUATION LENGTH WITH ITS OBTAINABLE
WORKSPACE AREA

Reachable region	L_1	L_2	L_3	L_4	L_5	L_6
Actuation length (mm)	5	10	15	20	25	30
Workspace area (mm²)	4	50	89	122	161	275

of desired stiffness/manipulability that best suit the given task. Therefore keeping all the parameters of the robot the same, while varying only the actuation length gives the plot in Fig. 4. For this analysis, the specification of the robot is given as $r_e = 0.5mm$, $r_b = 10r_e$, $l_i = 14r_e$, and $q_i = 66r_e$, which are all given with respect to the end effector radius.

Figure 4, shows the vertical $y-$axis plane cut of the robot workspace for a maximum arc length of $L = 30$mm. In addition, Table I presents the variation of reachable workspace area as a function of each corresponding actuation length. The reachable workspace/area is very small when the actuation length is 5mm (shown by the region below the yellow dotted line L_1) and this is because the robot cannot sustain any strain below $l_i = 3$mm. Therefore the non-reachable areas of the PCR within the given specifications are represented by the white-bounded region of the dotted cyan-colored line in Fig. 4. Another key issue is the instability of the robot configurations at the boundary regions, most especially for L_5 and L_6 due to low robot stiffness at these configurations, which causes an undesirable offset deviation (refer to Fig. 4). Therefore, care should be taken when designing and controlling a PCR, to ensure that output stiffness is sufficient for the desired tasks, as further design analysis and prototyping are mainly restricted to the fourth boundary region (L_4).

B. End effector dimension parameters

One of the key geometrical parameters of consideration, in designing a PCR is the dimension of the end effector. The end-effector couples the rods at the distal mobile end of the robot.

TABLE II
OBTAINABLE WORKSPACE AREA, MAXIMUM STIFFNESS,
MANIPULABILITY, AND ORIENTATION ANGLE DUE TO CHANGE OF
THE PCR END EFFECTOR DIMENSION

r_e (mm)	W-S (mm²)	$K_{z,mx}$ (N/mm)	$K_{y,mx}$ (N/mm)	$K_{x,mx}$ (N/mm)	κ max/min	Roll angle (degree)
$1.5r_b$	14.10	140	0.16	1.05	1.00/0.35	+57.5/-57.7
r_b	23.62	510	0.24	2.51	0.71/0.35	+72.7/-67.6
$0.5r_b$	33.41	150	0.79	2.84	0.45/0.19	+86.0/-75.7
$0.1r_b$	40.35	45	9.19	8.91	0.45/0.10	+89.8/-76.7

Although this part can be functionalized with actuators/sensors or manipulation tools, it is essential to understand the effect of change in the end-effector dimension as regards the manipulability, stiffness, reachable workspace, and obtainable end-effector orientation. To that effect, model analyses were carried out to investigate the effect of different end effector dimensions. For this particular analysis, only the end-effector dimension r_e is varied, whereas all other parameters of the robot are held constant. The robot specifications are $r_b = 2.5$mm, $l_i = 2r_b$, $q_i = 2r_b$, while the $r_e = [1.5, 1, 0.5, 0.1]r_b$ (refer to Fig. 5A). The comparative detail discussion for the three different robot configurations due to changes in the end effector dimension is analyzed below.

1) Workspace: the results of Fig. 5 show clearly the reachable workspace p_e of the robot in vertical $x-$axis plane when considering the variation of the end effector dimension. The reachable workspace area is presented in Table II for different end effector dimensions, which have a compound ratio of $1 : 1.67 : 2.37 : 2.86$. The variation of the end effector dimension on the obtainable workspace shows that a smaller end effector dimension results in a higher reachable workspace..

2) Stiffness: Fig. 5B, C, and D, represent the stiffness variation due to applied force in x-, y-, and z-direction respectively for the vertical x-axis plane. The stiffness values are computed as discussed in Subsection IVB above. Figure 5D, shows the result of the output stiffness for an applied force in the global z-axis direction. Considering the different robot configurations with various end-effector dimensions as presented in Table II, the maximum stiffness in the z-axis occurs when $r_e = r_b$. This agrees with the fact, that the lesser the stress on the robot links due to the end-effector constraint, the higher the stiffness or resistance to the applied force in the z-axis. The maximum stiffness for the y- and x-axis for each of the end effector dimensions are presented in Table II. The stiffness in y- and x-axis increases as the end effector dimension decreases (Fig. 5B and C). This can be related to the fact that the bigger the end effector, the higher the chances of perturbation with applied force in $x-$ and $y-$ directions. Whereas the smaller the end effector, the higher the stress resistance because the links are tightly constrained to a smaller area. Therefore, the influence of external forces is important to the resultant PCR design in terms of the robot's load-carrying capacity.

3) Manipulability: Fig. 5E relates to the manipulability of the robot configuration within the workspace as detailed under Subsection IVD. Though a smaller end effector PCR design, has the advantage of a large reachable workspace,
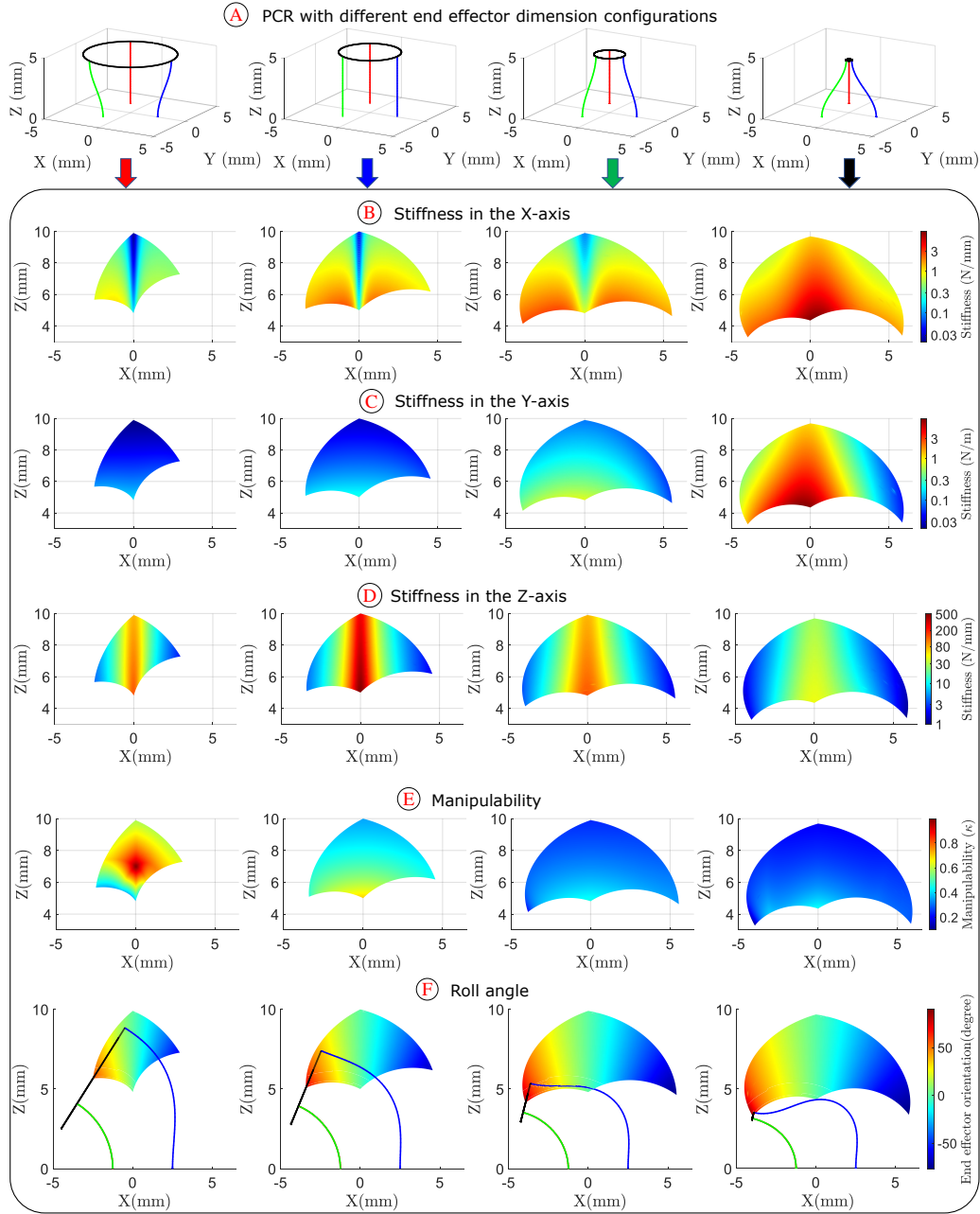
Fig. 5. Workspace vertical plane cut showing the effect of end effector geometrical parameters on the overall performance of the PCR in terms of stiffness, manipulability, and end-effector position and orientation. **A)** Robot shape for the different end effectors which are $r_e = [1.5, 1, 0.5, 0.1]r_b$, **B)** and **C)** are that of stiffness when the force is applied in the x- and y- axis respectively, **D)** Stiffness variation when the force is applied in the z-axis, **E)** Manipulability variation considering each end effector dimension, **F)** Obtainable end-effector orientation for each robot configuration.

the drawback becomes lower manipulability as shown in Fig. 5E. In essence, the bigger the end effector dimension, the higher the robot's dexterity for a given configuration (see Table II). Therefore, there is a compromise between the reachable workspace and the manipulability to ensure the efficient operation of the robot.

4) End effector orientation: Fig. 5F represents the end effectors rotation about the x-axis. Comparing the obtainable roll angle due to change in the end effector dimension shows that, the smaller the end effector, the higher the reachable roll angle just like that of the workspace. The maximum obtainable roll angle for each of the different end effector dimensions is

given in Table II. The higher roll angle associated with having a smaller end effector is linked to its ability to reach the higher boundary regions and having a larger workspace unlike in the case of a larger end effector dimension. In general, having a smaller end effector help to reach a tighter bending angle, which is desirable for most manipulators.

V. EXPERIMENTAL RESULTS

A. Prototype

The prototype of the proposed 3-leg miniaturized glass PCR is presented in Fig.1. It can be divided into 3 major aspects,
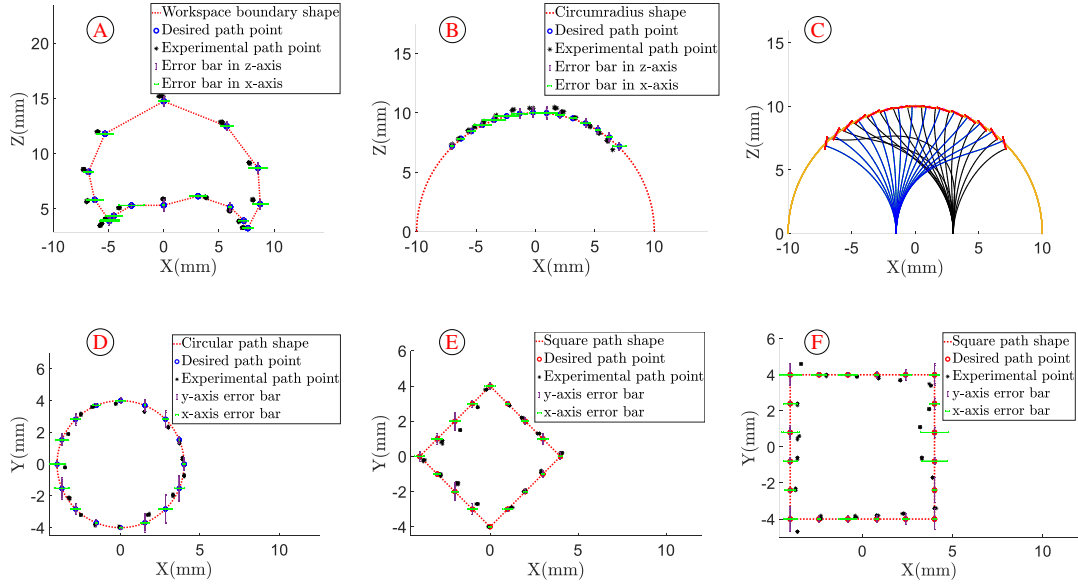
Fig. 6. Experimental validation: A) boundary workspace validation based on FKM, B) and C) circumradius validation along the 10 mm circular path using IKM in XZ plane, D) 8mm circular path, E) and F) square paths. Each path was evaluated at least four times and the error was computed for each point along the path.

which include: 1) the actuation unit 2) the parallel flexible structure, and 3) the controllers. The flexible part of the PCR is made of glass optical fibers, the vertical frame body support was fabricated by 3D print, while the actuation unit top and baseplate were done by laser cut. In general, the miniaturized glass PCR prototype has a compact structure with a simple design for rapid, miniaturized, and inexpensive fabrication. These are detailed below.

1) Actuation unit: The actuation unit has a height of 27mm and a circumradius of 14mm. The servomotors were placed in an equilateral triangular arrangement, so as to optimize space. Three holes of 300μm provide the guide support through which the optical glass fibers are deployed and also help to constrain the link below the baseplate top in a straight configuration.

The miniature linear servomotors used for this experiment are "*Spektrum RC 1.8 Gram Linear Ultra Micro Servo*", which have a maximal speed of 65mm/s, a stroke of 9.1mm and position repeatability of $\pm$0.14mm. Their size dimension is 8.2mm x 15mm x 16mm.

2) Flexible structure: The flexible part of the robot consists of a set of three optical fibers. This part also includes the distal rigid plate that couples together the optical fibers. For the robot prototype design, a standard glass optical fiber of diameter $125\mu m$ was used with a length of 6mm from the fixed base platform to the mobile end effector. The small end effector is a $500\mu m$ lightweight thickness carbon fiber plate.

3) Controller: The discrete pose of the robot is computed via the model on the computer using MATLAB which is connected to the Arduino board. In order to smoothen the motor acceleration and deceleration, an S-curve velocity profile for the generation of input control signal was implemented in the Arduino.

B. Workspace validation

The vertical $x-$axis plane for the workspace boundary validation of the miniature glass PCR is shown in Fig. 6A, for five repetitive movements. The FKM was used for the computation of the workspace boundary path. The validation of the boundary workspace as shown in Fig. 6A, has a mean error in x- and z-axis as 0.58mm and 0.28mm respectively. In addition, the standard deviation in the x- and z-axis is given as 0.29mm and 0.15mm respectively. The realized result shows the capability and flexibility of the robot to reach these extreme points within its boundary, without suffering fracture. This validates the FKM of the robot while considering extreme positions and one can see how close the results match.

C. IKM Validation

For the validation of the IKM, we carried out different path following that involves 1) a circumradius path movement in the vertical plane, 2) a circular path in the horizontal plane, and 3) two square paths. These are discussed in detail below.

1) Circumradius path: the IKM was used here to compute the circumradius path points on a radius of 10mm. Figure 6C, shows the side view of the simulation model for the different robot configurations. The validation result of this path shape is shown in Fig. 6B. It has a mean error in x- and z-axis as 0.25mm and 0.39mm respectively, while the standard deviation in x- and z-axis is gotten as 0.15mm and 0.23mm respectively. The result obtained shows how the robot follows the desired circular red line with a 10mm radius. It validates the modeling although the use of cheap servomotors.

2) Circular path: To further validate the robot IKM in a horizontal $z-$axis plane, a circular path tracing was demonstrated. To actualize this, a set of path points for the desired path within the robot workspace were computed using the

IKM. The result of the circular shape path is shown in Fig. 6D, which has a circular diameter of 8mm in x- and y-axis at a height of 5mm in z-axis. The error in $x-$ and y-axis was computed as 0.20mm and 0.31mm respectively, whereas the standard deviations in $x = 0.13$mm and in $y = 0.19$mm. The shape of the output result considering the end effector centroid position follows to some extent, the desired circular red line as shown in Fig. 6D. This validation result shows the accuracy of the IKM (shown by the error bar) and how close the experimental points follow the desired path.

3) Square path: Finally, two different square paths were used as shown in Fig. 6. The first square path (Fig. 6E), is a diagonal square within a circular diameter of 8mm. The diagonal vertices of the square are 8mm in both the x- and y-axis. The experimental validation gave a mean error in x and y as 0.18 and 0.20 respectively, while the standard deviation error is estimated as $x = 0.09$mm and $y = 0.13$mm. Next is the square path tracing with horizontal and vertical sides of 4mm in x- and y-axis (refer Fig. 6F). The realized experimental validation has a mean error in x- and y as 0.36mm and 0.29mm respectively and the standard deviation is gotten as $x = 0.22$mm and $y = 0.22$mm. For both cases, the experimental points which are the end effector centroid, tend to follow the desired square path with a considerable level of deviation. The various PCR validation results obtained are conclusive but limited by the use of cheap servomotors which have fairly low precision.

VI. Conclusion and Perspectives

One key challenge in micromanipulators with parallel architectures involves miniaturizing the robot size and having a large workspace. To overcome this huddle, we proposed a miniaturized glass PCR, particularly using a standard optics fiber of diameter 125μm. The design of the miniaturized glass PCR is characterized by high workspace volume, due to its structural design and kinematics. Compare to other micromanipulators with parallel structures in the literature, the miniaturized glass PCR has great potential for high scalability since the active parts are made of flexible rods and it has demonstrated a large workspace. Investigation of different geometrical parameters of the robot design was carried out. It was realized that smaller end effector PCR has a larger workspace in position and in orientation but consequently a lesser manipulability. The robot stiffness varies according to the robot's configuration and the direction of the applied force. The stiffness is larger when the force is applied z-axis compared to the $x-$ and y-axis and it is always maximum at the central bottom region while decreasing radially to the boundary end. We validated the robot FKM and IKM, adopted from the literature, by demonstrating the workspace boundary, path deployment, vertical plane circumradius path tracing, and horizontal plane circular and square path tracing operation. Future work includes the replacement of the miniature servomotors with better ones to improve the positioning repeatability, followed by an integration micro end effector for manipulation tasks. Finally, system uncertainty consideration and control will be achieved using visual servoing.

References

[1] L. Wu, R. Crawford, and J. Roberts, "Dexterity analysis of three 6-dof continuum robots combining concentric tube mechanisms and cable-driven mechanisms," IEEE Robotics and Automation Letters, vol. 2, no. 2, pp. 514–521, 2017.

[2] M. T. Chikhaoui, K. Rabenorosoa, and N. Andreff, "Kinematics and performance analysis of a novel concentric tube robotic structure with embedded soft micro-actuation," Mechanism and Machine Theory, vol. 104, pp. 234–254, 2016.

[3] Q. Peyron, Q. Boehler, P. Rougeot, P. Roux, B. J. Nelson, N. Andreff, K. Rabenorosoa, and P. Renaud, "Magnetic concentric tube robots: Introduction and analysis," The International Journal of Robotics Research, vol. 41, pp. 418 – 440, 2022.

[4] Z. Li, L. Wu, H. Ren, and H. Yu, "Kinematic comparison of surgical tendon-driven manipulators and concentric tube manipulators," Mechanism and Machine Theory, vol. 107, pp. 148–165, 2017.

[5] H. McClintock, F. Z. Temel, N. Doshi, J. sung Koh, and R. J. Wood, "The milliDelta: A high-bandwidth, high-precision, millimeter-scale delta robot," Science Robotics, vol. 3, no. 14, p. eaar3018, 2018.

[6] M. Leveziel, W. Haouas, G. J. Laurent, M. Gauthier, and R. Dahmouche, "Migribot: A miniature parallel robot with integrated gripping for high-throughput micromanipulation," Science Robotics, vol. 7, no. 69, p. eabn4292, 2022.

[7] C. E. Bryson and D. C. Rucker, "Toward parallel continuum manipulators," in 2014 IEEE International Conference on Robotics and Automation (ICRA), pp. 778–785, 2014.

[8] C. B. Black, J. Till, and D. C. Rucker, "Parallel continuum robots: Modeling, analysis, and actuation-based force sensing," IEEE Transactions on Robotics, vol. 34, no. 1, pp. 29–47, 2018.

[9] O. Altuzarra, D. Caballero, F. J. Campa, et al., "Position analysis in planar parallel continuum mechanisms," Mech. Mach. Theory, vol. 132, pp. 13–29, 2019.

[10] B. Mauze, R. Dahmouche, G. J. Laurent, A. N. Andre, P. Rougeot, P. Sandoz, and C. Clevy, "Nanometer Precision With a Planar Parallel Continuum Robot," IEEE Robotics and Automation Letters, vol. 5, pp. 3806–3813, July 2020.

[11] K. Nuelle, T. Sterneck, S. Lilge, D. Xiong, J. Burgner-Kahrs, and T. Ortmaier, "Modeling, Calibration, and Evaluation of a Tendon-Actuated Planar Parallel Continuum Robot," IEEE Robotics and Automation Letters, vol. 5, pp. 5811–5818, Oct. 2020.

[12] J. A. Rivera and C. J. Kim, "Spatial parallel soft robotic architectures," in IEEE/RSJ Int. Conf. on Intel. Rob. and Sys., pp. 548–553, 2014.

[13] G. Chen, Y. Kang, Z. Liang, Z. Zhang, and H. Wang, "Kinetostatics modeling and analysis of parallel continuum manipulators," Mech. Mach. Theory, vol. 163, p. 104380, 2021.

[14] O. F. Gallardo, B. Mauze, R. Dahmouche, C. Duriez, and G. J. Laurent, "Turning an Articulated 3-PPSR Manipulator into a Parallel Continuum Robot," in 2021 IEEE/RSJ International Conference on Intelligent Robots and Systems (IROS), pp. 4955–4960, 2021.

[15] A. L. Orekhov, C. B. Black, J. Till, S. Chung, and D. C. Rucker, "Analysis and Validation of a Teleoperated Surgical Parallel Continuum Manipulator," IEEE Robotics and Automation Letters, vol. 1, pp. 828–835, July 2016.

[16] V. Falkenhahn, A. Hildebrandt, R. Neumann, and O. Sawodny, "Model-based feedforward position control of constant curvature continuum robots using feedback linearization," in 2015 IEEE International Conference on Robotics and Automation (ICRA), pp. 762–767, 2015.

[17] A. AbuZaiter, E. L. Ng, M. S. M. Ali, and S. Kazi, "Miniature parallel manipulator using tinicu shape-memory-alloy microactuators," in 2015 10th Asian Control Conference (ASCC), pp. 1–4, 2015.

[18] J. Till, C. E. Bryson, S. Chung, A. Orekhov, and D. C. Rucker, "Efficient computation of multiple coupled Cosserat rod models for real-time simulation and control of parallel continuum manipulators," in 2015 IEEE International Conference on Robotics and Automation (ICRA), pp. 5067–5074, May 2015.

[19] S. Antman, Nonlinear Problems of Elasticity; 2nd ed. Dordrecht: Springer, 2005.

Chibundo J. Nwafor received a B.Eng. in Electrical/Electronics from Anambra State University, Uli, Nigeria, in 2012 and a Master Degree on Control for Green Mechatronics from Université Bourgogne Franche-Comté (UBFC), Besançon, France, in 2019. He is currently pursuing his PhD degree in Robotics at UBFC and is a member of the Automatic Control and Micro-Mechatronic Systems Department of FEMTO-ST Institute. His research interests include continuum robotics and micro-mechatronics systems for biomedical applications.

Guillaume J. Laurent received his Ph.D. in control systems and computer sciences from the University of Franche-Comté in France, in 2002. He is currently a professor at the National School of Mechanics and Microtechnologies (ENSMM) in Besançon. He is a member of the Automatic Control and Micro-Mechatronic Systems Department of FEMTO-ST Institute. His research interests include microrobotics, computer vision, parallel, and continuum robots.

Kanty Rabenorosoa received the M.S. degree in electrical engineering from Institut National des Sciences Appliquées Strasbourg, Strasbourg, France, in 2007, and the Ph.D. degree in automatic control from the University of FrancheComté, Besançon, France, in 2010. He was a Post-Doctoral Fellow at Laboratoire d'Informatique, de Robotique et de Micro-électronique de Montpellier, University of Montpellier, France, from 2011 to 2012. He is currently an Associate Professor with the AS2M Department, FEMTO-ST Institute, Besançon. His research interests include mechatronics, smart actuator, soft and continuum microrobotics for medical applications within the Automatic Control and Micro-Mechatronic Systems Department.